

Inertial two- and three-dimensional thin film flow over topography

S. Veremieiev, H.M. Thompson, Y.C. Lee, P.H. Gaskell

School of Mechanical Engineering, The University of Leeds, Leeds, United Kingdom, LS2 9JT.

Abstract

The effect of inertia on gravity-driven thin film free-surface flow over substrates containing topography is considered. Flow is modelled using a depth-averaged form of the governing Navier-Stokes equations and the discrete analogue of the coupled equations solved accurately using an efficient full approximation storage (FAS) algorithm and a full multigrid (FMG) technique. The effect of inertia on free-surface disturbances induced by topographic features is illustrated by considering examples of gravity-driven flow over and around peak, trench and occlusion topography. Results are given which demonstrate how increasing Reynolds number can significantly enhance the magnitude of free-surface disturbances induced, a feature which may have important consequences for the wide range of coating processes which aim to maximise free-surface planarity.

Keywords: coating, thin film flows, microfluidics, topography

1. Introduction

The deposition of thin film coatings over substrates containing regions of micro-scale topography and occlusions forms an important component of many natural and scientific processes [1], in substrate cooling and heat transfer applications [2,3], and several precision manufacturing techniques. Examples of the latter can be found in the production of anti-reflective coatings, [4], flexible electronic components [5], and in displays and sensors [6], where thin liquid films flow over a distribution of functional topographical features such as light-emitting species on a screen. In industrial coating applications product functionality often depends critically on the coated film thickness distribution and this has stimulated much interest in recent years on understanding the flow mechanisms controlling free-surface disturbances induced by topographic features.

The present lack of reliable data is testament to the difficulties of studying such systems experimentally, so numerical simulations are likely to be the most viable option in the foreseeable future. Most previous numerical studies of thin film flow over topography have been carried out using lubrication theory, an approach that has proven to be surprisingly accurate when compared against the scant experimental data that is currently available. However, the effects of inertia can also be influential in practical coating flows: recent studies of two-dimensional film flow over topography have shown how increasing inertia amplifies the free surface disturbances induced by topography [7,8] and can lead to free surface instabilities when the Reynolds number exceeds a critical value [9,10]. See also the analysis in [11] and [12] concerning resonance effects in viscous film flow over inclined wavy substrates.

The focus of the present study is different to the above and analyses the interplay between inertial and topographical influences on three-dimensional free-surface disturbances induced by thin film flow over and around substrate topography. The approach adopted involves the efficient solution of a depth-averaged form of the governing Navier-Stokes equations [13]. Section 2 formulates the flow problems of interest while Section 3 outlines the numerical solution

27 method adopted. Results are presented in Section 4 for the influence of inertia on free-surface
 28 disturbances induced by flow over combinations of submerged peak and trench topographies
 29 and past a regular square occlusion. Conclusions are drawn in Section 5.

30 2. Problem Formulation

31 The problems of interest, shown schematically in Figure 1, are of gravity-driven film flow
 32 down a planar surface containing either a square submerged topography of height S_0 (Figure
 33 1a) or occlusion (Figure 1b) of length L_T ($\ll L_P$), width W_T ($\ll W_P$), where L_P and W_P are
 34 length and width of the problem domain respectively. The liquid is assumed to be Newtonian
 35 and incompressible, with constant viscosity, μ , density, ρ , and surface tension σ . The chosen
 36 Cartesian streamwise, X , spanwise, Y , and normal, Z , coordinates are as indicated and the
 37 solution domain is bounded from below by the inclined surface $S(X, Y)$ and from above at time
 38 T by the free-surface $F(X, Y, T)$. The film thickness, $H(X, Y, T)$, at any point in the (X, Y)
 39 plane is given by $H = F - S$ and the resulting laminar flow is described by the Navier-Stokes
 40 and continuity equations, namely:

$$\rho \left(\frac{\partial \mathbf{U}}{\partial T} + \mathbf{U} \cdot \nabla \mathbf{U} \right) = -\nabla P + \nabla \cdot \mathbf{T} + \rho \mathbf{G}, \quad (1)$$

$$\nabla \cdot \mathbf{U} = 0, \quad (2)$$

42 where $\mathbf{U} = (U, V, W)$ and P are the fluid velocity and pressure, respectively;
 43 $\mathbf{T} = \mu \left(\nabla \mathbf{U} + (\nabla \mathbf{U})^T \right)$ is the viscous stress tensor and $\mathbf{G} = g_0 (\sin \theta, 0, -\cos \theta)$ is the ac-
 44 celeration due to gravity where g_0 is the standard gravity constant.

45 Taking the reference length-scale in all directions to be the asymptotic, or fully devel-
 46 oped, film thickness, H_0 , and scaling the velocities by the free-surface (maximum) velocity,
 47 $U_0 = \rho g_0 H_0^2 \sin \theta / 2\mu$ apropos the classic Nusselt solution [14], pressure (stress tensor) by
 48 $P_0 = \mu U_0 / H_0$, and time by $T_0 = H_0 / U_0$, equations (1) and (2) can be rewritten in non-
 49 dimensional form as:

$$\text{Re} \left(\frac{\partial \mathbf{u}}{\partial t} + \mathbf{u} \cdot \nabla \mathbf{u} \right) = -\nabla p + \nabla \cdot \boldsymbol{\tau} + \text{St} \mathbf{g}, \quad (3)$$

$$\nabla \cdot \mathbf{u} = 0, \quad (4)$$

51 where $\mathbf{u} = (u, v, w)$, $\boldsymbol{\tau}$ and $\mathbf{g} = \mathbf{G} / g_0$ are the dimensionless velocity, viscous stress tensor and
 52 gravity component, respectively; $\text{Re} = \rho U_0 H_0 / \mu$ is the Reynolds number and $\text{St} = 2 / \sin \theta$ the
 53 Stokes number.

54 The problem is closed by imposing the required no-slip, inflow/outflow, kinematic, free-
 55 surface normal and tangential stress boundary conditions, namely:

$$\mathbf{u}|_{z=s} = 0, \quad (5)$$

$$\mathbf{u}|_{x=0, l_p; y=0, w_p} = (z(2-z), 0, 0), \quad (6)$$

$$\frac{\partial f}{\partial t} + u|_{z=f} \frac{\partial f}{\partial x} + v|_{z=f} \frac{\partial f}{\partial y} - w|_{z=f} = 0, \quad (7)$$

$$-p + (\boldsymbol{\tau}|_{z=f} \cdot \mathbf{n}_f) \cdot \mathbf{n}_f = \frac{\kappa}{\text{Ca}}, \quad (8)$$

$$(\boldsymbol{\tau}|_{z=f} \cdot \mathbf{n}_f) \cdot \mathbf{t}_f = 0, \quad (9)$$

60 where $\text{Ca} = \mu U_0 / \sigma$ is the capillary number, $x, y, z, l_p, w_p, s, h, f$ correspond to their dimensional
61 counterparts, $\mathbf{n}_f = \left(-\frac{\partial f}{\partial x}, -\frac{\partial f}{\partial y}, 1 \right) \cdot \left[\left(\frac{\partial f}{\partial x} \right)^2 + \left(\frac{\partial f}{\partial y} \right)^2 + 1 \right]^{-1/2}$ is the unit normal vector pointing
62 outward from the free surface, \mathbf{t}_f is the unit vector tangential to the free surface and $\kappa = -\nabla \cdot \mathbf{n}_f$
63 is the free-surface curvature.

64 For the occlusion problem, Figure 1b, the liquid meets the occlusion at a static contact line
65 with a resulting static contact angle, θ_S , formed at the free-surface in a plane normal to the
66 occlusion boundary. Following [15], this condition together with a no-slip boundary condition
67 at the boundary of the occlusion Γ are imposed via

$$\nabla h|_{(x,y) \in \Gamma} \cdot \mathbf{n}_\Gamma = \tan \left(\theta_S - \frac{\pi}{2} \right), \quad (10)$$

$$\mathbf{u}|_{(x,y,z) \in \Gamma} = 0, \quad (11)$$

69 where \mathbf{n}_Γ is the outward pointing normal to the occlusion.

70 2.1. Mathematical formulation

71 Since the mathematical details are described in detail in [13], only a very brief overview is
72 provided. A process of depth-averaging is used by adopting a long-wave approximation that
73 $\varepsilon = H_0 / L_0 \ll 1$, where $L_0 = H_0 / (6\text{Ca})^{1/3}$ is the characteristic in-plane capillary length scale.
74 The required friction and dissipation terms are obtained by assuming the self-similar velocity
75 profiles:

$$u = 3\bar{u} (\xi - 1/2\xi^2), \quad v = 3\bar{v} (\xi - 1/2\xi^2), \quad (12)$$

76 where $\xi = (z - s) / h$. Then the depth-averaged form (DAF) of the momentum equations (3)
77 and the continuity equation (4) for the unknown averaged velocities $\bar{u}(x, y, t) = \frac{1}{h} \int_s^f u \, dz$,
78 $\bar{v}(x, y, t) = \frac{1}{h} \int_s^f v \, dz$ and the film thickness $h(x, y, t)$ respectively are:

$$\varepsilon \text{Re} \left[\frac{\partial \bar{u}}{\partial t} - \frac{\bar{u}}{5h} \frac{\partial h}{\partial t} + \frac{6}{5} \left(\bar{u} \frac{\partial \bar{u}}{\partial x} + \bar{v} \frac{\partial \bar{u}}{\partial y} \right) \right] = \frac{\partial}{\partial x} \left[\frac{\varepsilon^3}{\text{Ca}} \nabla^2 f - 2\varepsilon f \cot \theta \right] - \frac{3\bar{u}}{h^2} + 2, \quad (13)$$

$$\varepsilon \text{Re} \left[\frac{\partial \bar{v}}{\partial t} - \frac{\bar{v}}{5h} \frac{\partial h}{\partial t} + \frac{6}{5} \left(\bar{u} \frac{\partial \bar{v}}{\partial x} + \bar{v} \frac{\partial \bar{v}}{\partial y} \right) \right] = \frac{\partial}{\partial y} \left[\frac{\varepsilon^3}{\text{Ca}} \nabla^2 f - 2\varepsilon f \cot \theta \right] - \frac{3\bar{v}}{h^2}, \quad (14)$$

$$\frac{\partial h}{\partial t} + \frac{\partial}{\partial x} (h\bar{u}) + \frac{\partial}{\partial y} (h\bar{v}) = 0. \quad (15)$$

81 Problems are closed using averaged forms for the outflow/inflow conditions and the assump-
82 tion of fully developed flow both upstream and downstream, namely:

$$\bar{u}|_{x=0} = 2/3, \quad \bar{v}|_{x=0} = \frac{\partial \bar{u}}{\partial x}|_{x=l_p} = \frac{\partial \bar{v}}{\partial x}|_{x=l_p} = \frac{\partial \bar{u}}{\partial y}|_{y=0, w_p} = \frac{\partial \bar{v}}{\partial y}|_{y=0, w_p} = 0, \quad (16)$$

$$h|_{x=0} = 1, \quad \frac{\partial h}{\partial x}|_{x=l_p} = \frac{\partial h}{\partial y}|_{y=0, w_p} = 0. \quad (17)$$

84 In addition the occlusion problem requires the static contact line and no-slip conditions

$$\varepsilon \nabla h|_{(x,y) \in \Gamma} \cdot \mathbf{n}_\Gamma = \tan \left(\theta_S - \frac{\pi}{2} \right), \quad \bar{u}|_{(x,y) \in \Gamma} = \bar{v}|_{(x,y) \in \Gamma} = 0. \quad (18)$$

2.2. Topography Definition

Attention is restricted to flows involving simple, well-defined square peak, trench and occlusion topographies. Since, for submerged peak and trench topography, their profile appears as a function in the governing equations, it is not possible to consider completely sharp features. Following previous studies [16], the peak and trench topographies are specified via arctangent functions defined as follows:

$$s(x^*, y^*) = \frac{s_0}{4 \tan^{-1} \frac{l_t}{2\delta} \tan^{-1} \frac{w_t}{2\delta}} \left[\tan^{-1} \left(\frac{x^* + l_t/2}{\delta} \right) - \tan^{-1} \left(\frac{x^* - l_t/2}{\delta} \right) \right] \\ \times \left[\tan^{-1} \left(\frac{y^* + w_t/2}{\delta} \right) - \tan^{-1} \left(\frac{y^* - w_t/2}{\delta} \right) \right], \quad (19)$$

where s_0 is the dimensionless depth ($s_0 < 0$) or height ($s_0 > 0$), with l_t, w_t and δ the non-dimensional streamwise length, spanwise width and steepness factor, respectively. The coordinate system $(x^*, y^*) = (x - x_t, y - y_t)$ has its origin at the centre of the topography, (x_t, y_t) .

3. Method of Solution

Since the method of solution is based on that described in detail in [13], only a brief outline is given below.

3.1. Spatial Discretisation

Equations (13) to (15), incorporating appropriate friction and dispersion terms, are solved subject to the applicable boundary conditions on a rectangular computational domain, $(x, y) \in \Omega = (0, l_p) \times (0, w_p)$, subdivided using a regular spatially staggered mesh arrangement of cells having sides of length Δx and width Δy . The unknown variables, film thickness, h , and the velocity components, \bar{u} , \bar{v} , are located at cell centres, (i, j) , and cell faces, $(i + 1/2, j)$, $(i, j + 1/2)$, respectively. Solving the momentum equations (13) and (14) at cell faces with the convection and time derivative terms grouped together to simplify their numerical treatment, and omitting for the sake of convenience the overbar denoting velocity averaging, results in the following second-order accurate (in space) finite difference scheme:

$$\varepsilon \text{Re} \left(\frac{\partial u}{\partial t} - \frac{u}{5h} \frac{\partial h}{\partial t} + \frac{6}{5} F[u] \right)_{i+1/2, j} \\ - \frac{\varepsilon^3}{\text{Ca}} \left(\frac{f_{i+1, j+1} - 2f_{i+1, j} + f_{i+1, j-1} - f_{i, j+1} + 2f_{i, j} - f_{i, j-1}}{\Delta x \Delta y^2} \right. \\ \left. + \frac{f_{i+2, j} - 3f_{i+1, j} + 3f_{i, j} - f_{i-1, j}}{\Delta x^3} \right) + 2\varepsilon \cot \theta \frac{f_{i+1, j} - f_{i, j}}{\Delta x} + \frac{3u_{i+1/2, j}}{h_{i+1/2, j}^2} - 2 = 0, \quad (20)$$

$$\varepsilon \text{Re} \left(\frac{\partial v}{\partial t} - \frac{v}{5h} \frac{\partial h}{\partial t} + \frac{6}{5} F[v] \right)_{i, j+1/2} \\ - \frac{\varepsilon^3}{\text{Ca}} \left(\frac{f_{i+1, j+1} - 2f_{i, j+1} + f_{i-1, j+1} - f_{i+1, j} + 2f_{i, j} - f_{i-1, j}}{\Delta x^2 \Delta y} \right. \\ \left. + \frac{f_{i, j+2} - 3f_{i, j+1} + 3f_{i, j} - f_{i, j-1}}{\Delta y^3} \right) + 2\varepsilon \cot \theta \frac{f_{i, j+1} - f_{i, j}}{\Delta y} + \frac{3v_{i, j+1/2}}{h_{i, j+1/2}^2} = 0, \quad (21)$$

$$\frac{\partial h_{i, j}}{\partial t} + \frac{h_{i+1/2, j} u_{i+1/2, j} - h_{i-1/2, j} u_{i-1/2, j}}{\Delta x} + \frac{h_{i, j+1/2} v_{i, j+1/2} - h_{i, j-1/2} v_{i, j-1/2}}{\Delta y} = 0, \quad (22)$$

114 where $F[\omega] = u \frac{\partial \omega}{\partial x} + v \frac{\partial \omega}{\partial y}$ is the convective operator and the following terms are interpolated from
 115 neighbouring nodes: $h_{i\pm 1/2,j} = (h_{i\pm 1,j} + h_{i,j})/2$, $h_{i,j\pm 1/2} = (h_{i,j\pm 1} + h_{i,j})/2$. The convective
 116 operator $F[\omega]$ is discretized using a second-order accurate total variation diminishing (TVD)
 117 scheme [17].

118 3.2. Temporal Discretisation

119 The associated time discretisation includes the use of an explicit and second-order accurate
 120 in time predictor and a semi-implicit β -method [17] solution stages. For $\beta = 1/2$ the method
 121 reduces to the second order accurate in time, but conditionally stable Crank-Nicolson scheme,
 122 whereas $\beta = 1$ leads to the fully implicit first order accurate in time unconditionally stable Laa-
 123 sonen method. The automatic adaptive time-stepping procedure adopted employs an estimate
 124 of the local truncation error (LTE) obtained from the difference between an explicit predic-
 125 tor stage and the current solution stage to optimise the size of time steps and thus minimise
 126 computational waste.

127 3.3. Multigrid Solver

128 The discretized equations are solved using a multigrid strategy with a combined Full Ap-
 129 proximation Storage (FAS) and full multigrid (FMG) technique, where errors on a partic-
 130 ular computational grid are reduced by employing a hierarchy of successively finer grids,
 131 $G^0, \dots, G^k, \dots, G^K$, where G^0 denotes the coarsest and G^K the finest grid level. The FMG
 132 solution process consists of performing a fixed number of FAS V-cycles on intermediate grid
 133 levels $G^k \in [G^1, \dots, G^{k-1}]$ (usually 1-3 V cycles) and up to 10 V cycles on the finest grid level G^K .
 134 Due to the staggered nature of the discretization involved, the relaxation methodology adopted
 135 employs a lexicographic box smoothing Gauss-Seidel scheme. Dirichlet boundary conditions
 136 are assigned as exact values at the boundary points, whereas Neumann boundary conditions
 137 are implemented by employing ghost nodes at the edge of the computational domain.

138 4. Results

139 Results are provided which briefly explore the effect of Reynolds number on the resultant
 140 free surface disturbance for gravity-driven thin film flow over an inclined substrate with $\theta = \frac{\pi}{6}$,
 141 $\theta_S = \frac{\pi}{2}$ and $\varepsilon = 0.1$, which results in $\text{Ca} = \varepsilon^3/6 = 0.000167$. For three-dimensional flow, the
 142 two-dimensional flow domain has $l_p = w_p = 80$ and the topography has $l_t = w_t = 1.0$ and is
 143 centred at $(x_t, y_t) = (30, 40)$, while for two-dimensional flow, the one-dimensional flow domain
 144 has $l_p = 80$, $l_t = 1.0$ and $x_t = 40$; in all cases $\delta = 0.001$. The multigrid algorithm employs a
 145 coarsest grid level G^0 with $n_x^0 = n_y^0 = 64$ ($n_x^0 = 64$ in one-dimension) and a finest grid level G^4
 146 with $n_x^4 = n_y^4 = 1024$ (G^5 with $n_x^5 = 2048$ in one-dimension) uniformly spaced cells. Steady-
 147 state solutions are generated by solving the time-dependent equations (20) to (22) starting from
 148 an initially flat free surface, $f = 1$, with velocities $u = \frac{2}{3}h^2$, $v = 0$ (commensurate with $\text{Re} = 0$)
 149 at $t = 0$. At each time step sufficient multigrid V-cycles are performed to reduce residuals on
 150 the finest mesh level to below 10^{-6} .

151 Figure 2 shows the effect of inertia on the flow over a spanwise (i.e. one-dimensional) peak
 152 topography. The free-surface disturbance is characterised by an upstream depression followed
 153 by a large amplification over the peak topography. Increasing Re in this case leads to an
 154 enhancement in the magnitude of the free-surface peak from $f = 1.14$ for $\text{Re} = 5$ to $f = 1.16$
 155 for $\text{Re} = 50$, with a similar increase in magnitude in the corresponding upstream free-surface
 156 depression. Figure 3 considers inertial flow over a two-dimensional localised peak topography
 157 which leads to a three-dimensional free-surface disturbance. In this case increasing Re from 5
 158 to 50 leads to a similar enhancement and widening of the free-surface disturbance, where the

159 characteristic capillary ridge and downstream surge reported for flow over a trench topography
160 [15] have been replaced by two small free-surface depressions. These features are shown more
161 clearly in the streamwise and spanwise free-surface profiles for $5 \leq \text{Re} \leq 50$ shown in Figure
162 4. Note that the downstream free-surface depressions shown in Figure 4(a) only occur in
163 three-dimensional flows and result from spanwise flow away from the streamwise topography
164 centreline.

165 For low Reynolds number flows [18] suggested that linear superposition of the free-surface
166 responses to elementary topographies can reliably construct the response for more complex and
167 realistic topography patterns. Figure 5 considers the effect of inertia and submerged topography
168 magnitude $|s_0|$ on the superposition of free-surface disturbances. It shows streamwise free-
169 surface profiles through the centre of the topography for three-dimensional flow over submerged
170 peak and trench topographies with $|s_0| = 0.1$ and 0.25 and $\text{Re} = 5$ and 50 . Also shown are
171 the superposed profiles that result by adding together the individual profiles for the peak
172 and trench topographies; the profiles are scaled by depth/height of the topography as $f^* =$
173 $(f - 1) / |s_0|$. Note that linear responses to topography profiles would result in completely flat
174 superposed profiles. For the smaller amplitude topography cases, with $|s_0| = 0.1$, increasing
175 Re from 5 to 50 leads to the peak of the superposed profile increasing from 8% to 18% of the
176 average magnitude of the individual free-surface disturbance profiles. For $|s_0| = 0.25$, these
177 values increase further to 19% and 45% respectively. This data clearly shows that the free-
178 surface response to submerged topography becomes, as expected, increasingly non-linear as Re
179 is increased.

180 The final figures, 6 and 7, consider the effect of replacing the submerged square peak/trench
181 topography by a corresponding square occlusion that is much taller than the characteristic film
182 thickness. In this case, increasing Re from 5 to 50 leads to a doubling of the free-surface
183 disturbance upstream of the occlusion with the result that the local film thickness is increased
184 from $h = 1.09$ for $\text{Re} = 5$ to $h = 1.20$ for $\text{Re} = 50$. Inertia also has an impact on the degree
185 of film thinning downstream of the occlusion: increasing Re from 5 to 50 increases the degree
186 of film thinning from approximately $h = 0.98$ to $h = 0.93$. As noted by [2] knowledge of such
187 localised film thickness variations is very important in, for example, cooling applications since
188 they can have a major impact on the achievable heat transfer rates into cooling films.

189 5. Conclusions

190 In addition to its well-known influence on free-surface stability, this paper has shown that
191 inertia can cause amplification and enhancement of free-surface disturbances that result from
192 flow over and around surface topography. The precise form of the disturbance is affected by the
193 nature of the topography (spanwise or localised, submerged or occlusion). Increasing inertia
194 causes the free-surface response to submerged topography to become non-linear and can cause
195 significant local variations in film thickness in the vicinity of localised occlusions. The ability
196 to predict and control both of these features is beneficial in coating applications where the goal
197 is often that of ensuring predictable product properties by accurate control of film thickness
198 variations within coated films.

199 6. Acknowledgement

200 S. Veremieiev gratefully acknowledges the financial support of the European Union Marie
201 Curie Action, contract MEST-CT-2005-020599.

7. References

- [1] S.J. Abbott and P.H. Gaskell, Mass production of bio- inspired structured surfaces, Proc. IMechE, Part C: J. Mech. Eng. Sci., 221(2007) 1181-1191.
- [2] S.J. Baxter, H. Power, K.A. Cliffe and S. Hibberd, Three-dimensional thin film flow over and around an obstacle on an inclined plane, Phys. Fluids, 21(3)(2009) 032102-032102-23,.
- [3] K. Helbig, R. Nasarek, T. Gambaryan-Roisman and P. Stephan, Effect of longitudinal microgrooves on flow stability and wave characteristics of falling liquid films, J. Heat Transfer, 131(1)(2009) 011601-011608,
- [4] N.C. Linn, C.-H. Sun, P. Jiang and B. Jiang, Self-assembled biomimetic antireflection coatings, Appl. Phys. Lett., 91(2007) 101108.
- [5] H.C. Ko, M.P. Stoykovich, J. Song, V. Malyarchuk, W.M. Choi, C.-J. Yu, J.B. Geddes, J. Xiao, Y. Huang and J.A.A. Rogers, A hemispherical electronic eye camera based on compressible silicon optoelectronics, Nature, 454(2008) 748-753.
- [6] M.M.J. Decré and J.C. Baret, Gravity-driven flows of viscous liquids over two-dimensional topographies., J. Fluid Mech., 487(2003), 147-166.
- [7] S. Saprykin, R.J. Koopmans and S. Kalliadasis, Free-surface thin-film flows over topography: influence of inertia and viscoelasticity, J. Fluid Mech., 578(2007), 271-293.
- [8] V. Bontozoglou and K. Serifi, Falling film flow along steep two-dimensional topography: The effect of inertia, Int. J. Mult. Flow, 34(2008), 734-747.
- [9] R.V. Craster and O.K. Matar, Dynamics and stability of thin liquid films, Rev. Mod. Phys., 81(3)(2009), 1131-1198.
- [10] A. Wierschem and N. Aksel, Instability of a liquid film flowing down an inclined wavy plane, Physica D., 186(3-4)(2003), 221-237.
- [11] A. Wierschem, V. Bontozoglou, C. Heining, H. Uecker and N. Aksel, Linear resonance in viscous films on inclined wavy planes, Int. J. Multiphase Flow, 34(6)(2008), 580-589.
- [12] C. Heining, V. Bontozoglou, N. Aksel and A. Wierschem, Nonlinear resonance in viscous films on inclined wavy planes, Int. J. Multiphase Flow, 35(1)(2009), 78-90.
- [13] S. Veremieiev, H.M. Thompson, Y.C. Lee, and P.H. Gaskell, Inertial thin film flow on planar surfaces featuring topography. Comp. & Fluids, 39(3)(2010), 431-450.
- [14] J.H. Spurk, and N. Aksel, Fluid Mechanics., Academic Press, Springer (2008).
- [15] M. Sellier, Y.C. Lee, H.M. Thompson and P.H. Gaskell, Thin film flow on surfaces containing arbitrary occlusions, Computers & Fluids, 38(2009), 171-182.
- [16] P.H. Gaskell, P.K. Jimack, M. Sellier, H.M. Thompson, and M.C.T. Wilson, Gravity-driven flow of continuous thin liquid films on non-porous substrates with topography, J. Fluid Mech., 509(2004), 253-280.
- [17] T.J. Chung, Computational Fluid Dynamics., Cambridge University Press: Cambridge (2002).
- [18] M. Hayes, S.B.G. O'Brien and J.H. Lammers, Green's function of a steady flow over a two-dimensional topography, Phys. Fluids, 12 (2000), 2845-2858.

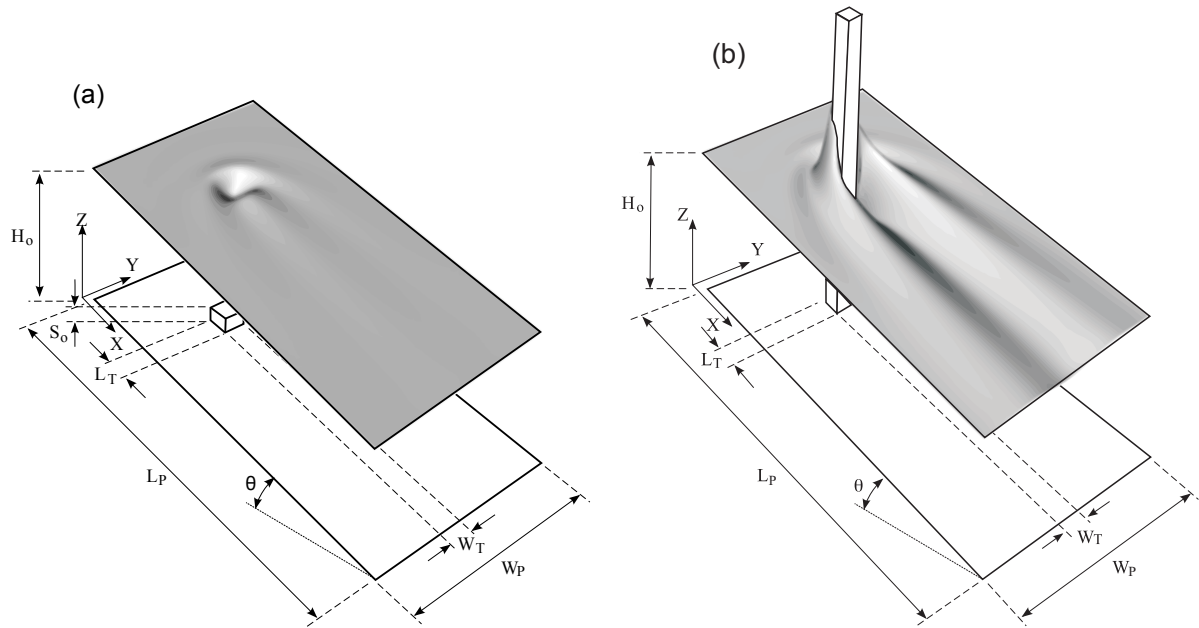


Figure 1: Schematic of gravity-driven film flow over topography: (a) over a square submerged peak and (b) past an occlusion.

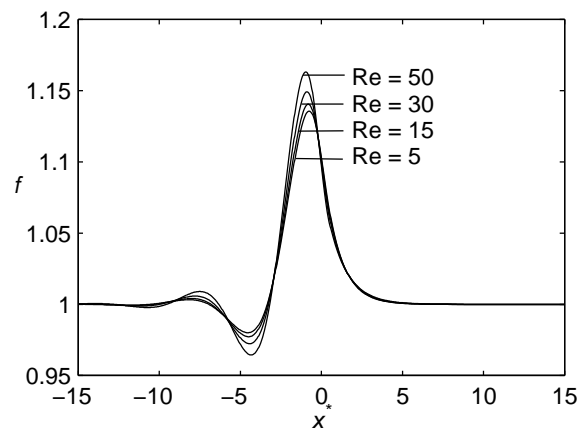


Figure 2: Effect of Re on the free-surface profile for flow over a spanwise peak topography, $s_0 = 0.25$.

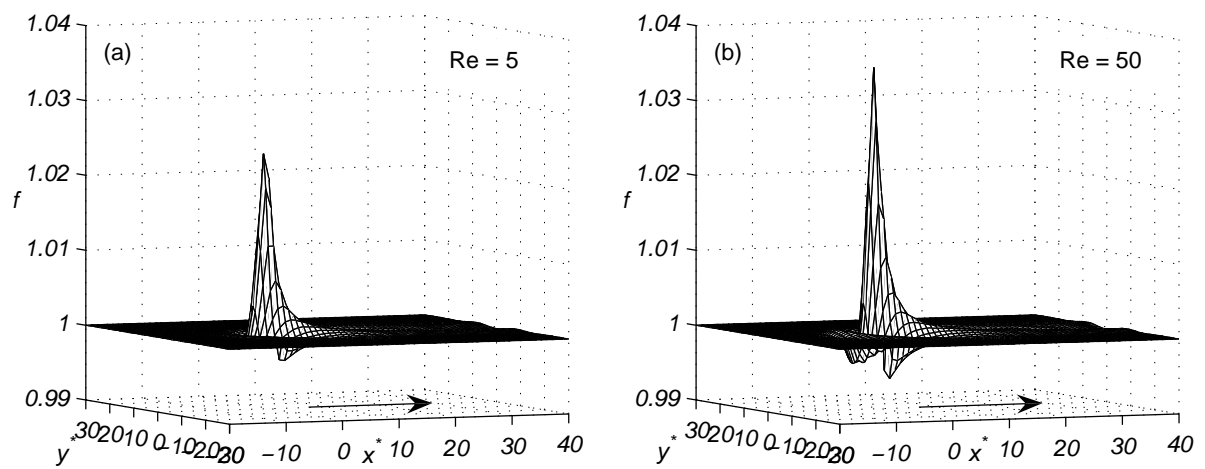


Figure 3: Free-surface plot for flow over a two-dimensional localised square peak topography with $s_0 = 0.25$: (a) $Re=5$; (b) $Re=50$.

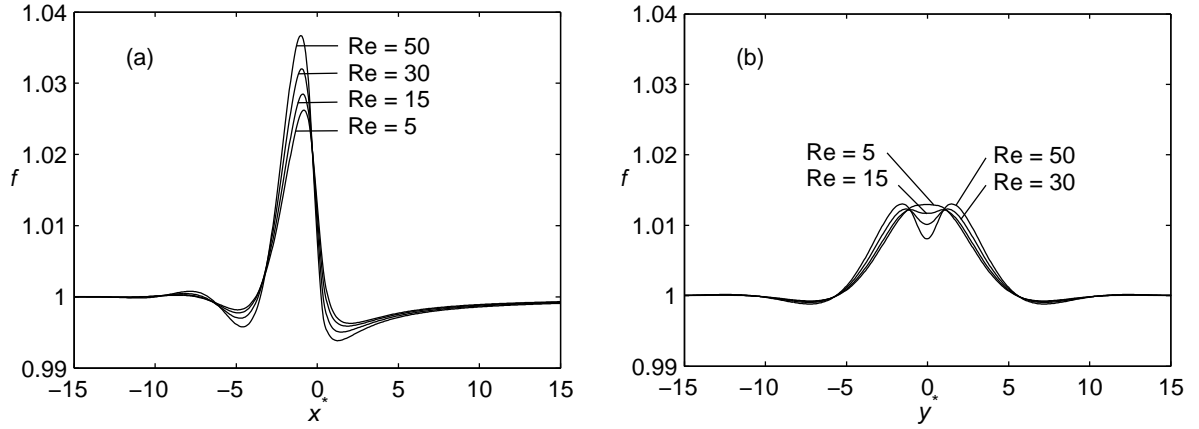


Figure 4: Effect of Re on (a) the streamwise and (b) the spanwise free-surface profile along the centre-lines through a localised peak topography, $s_0 = 0.25$.

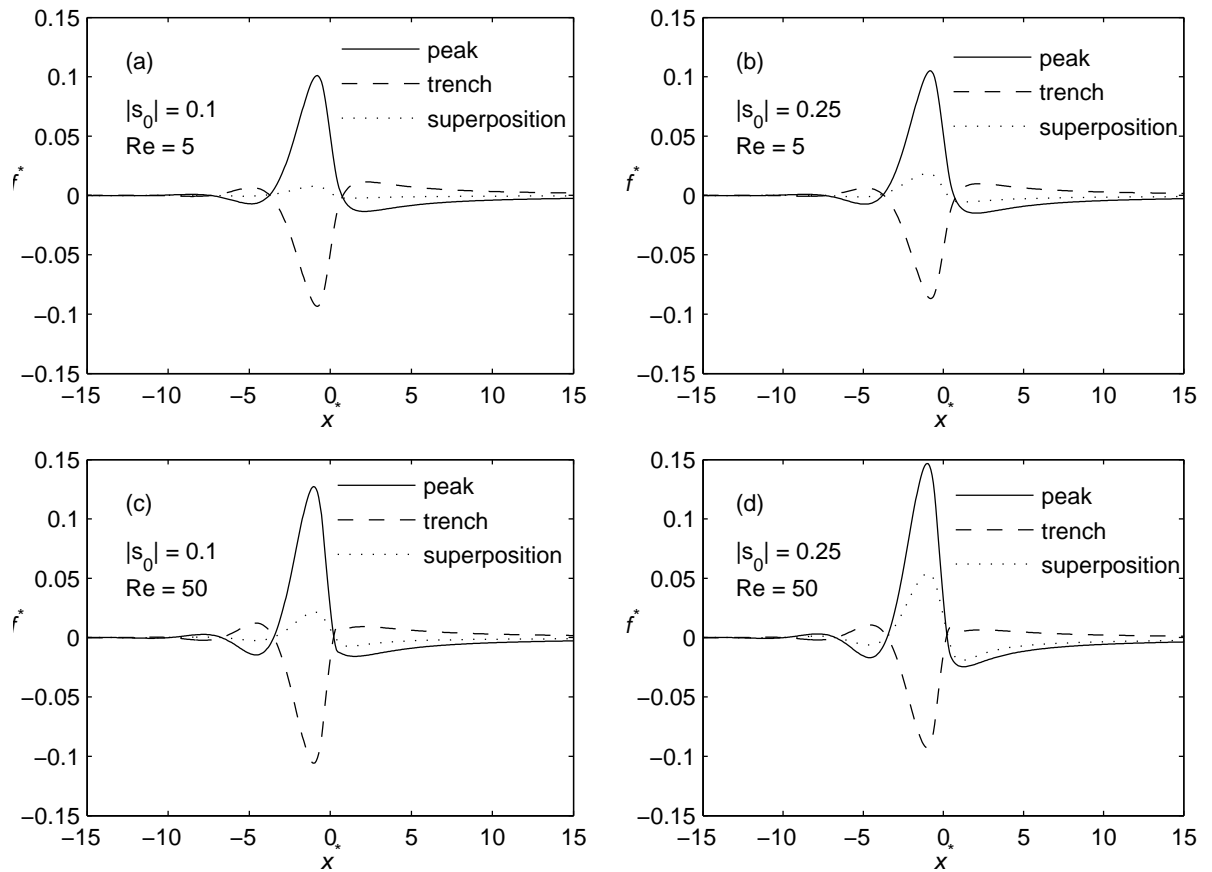


Figure 5: Superposition of streamwise centre-line free-surface profiles for flow over localised trench and peak topographies having equal but opposite depth/height, $|s_0| = 0.1$ (left) and 0.25 (right): $Re = 5$ (top) and 50 (bottom).

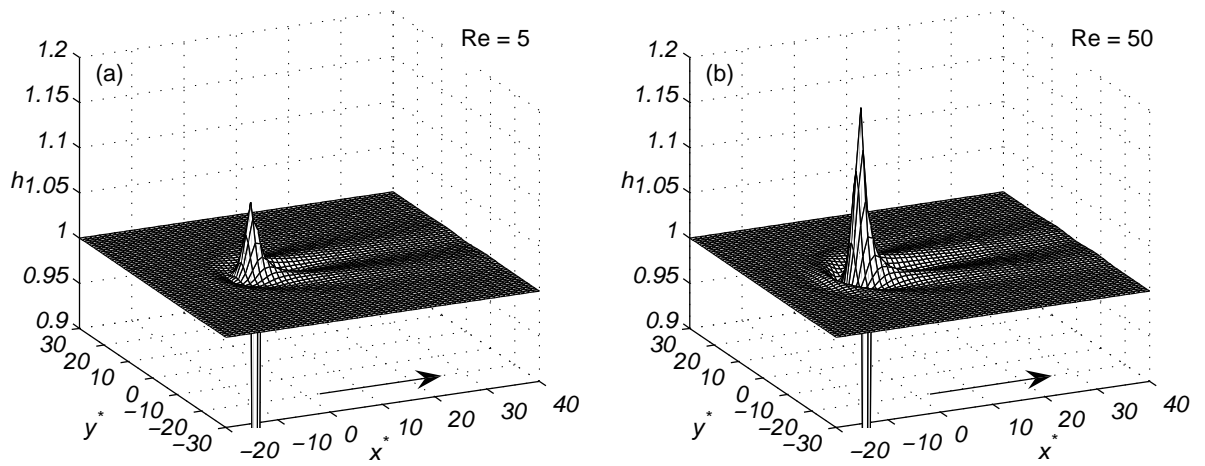


Figure 6: Free-surface plot for flow around a two-dimensional localised square occlusion: (a) $Re = 5$; (b) $Re = 50$.

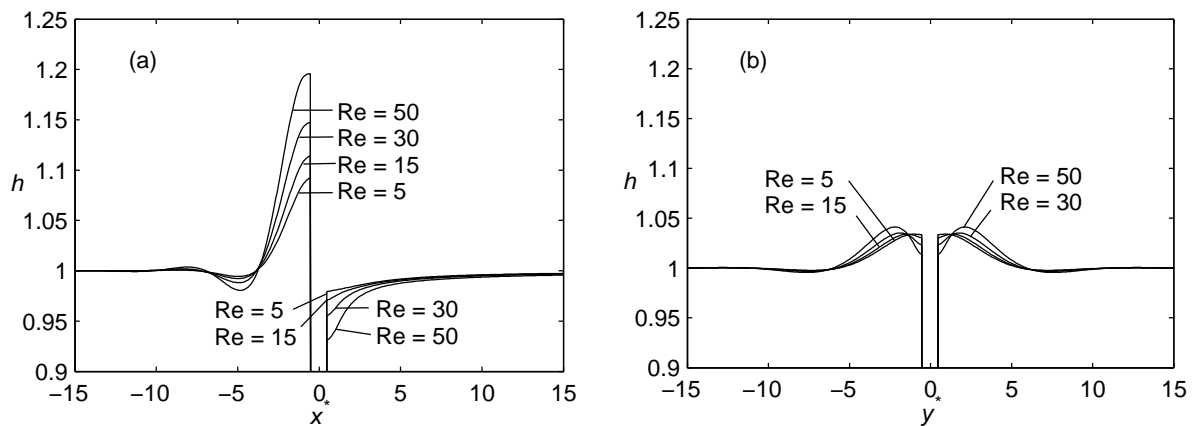


Figure 7: Effect of Re on (a) the streamwise and (b) the spanwise free-surface profile along the centre-lines through a localised square occlusion.